Supplementary Information

Lipstick structure revealed by multimodal strain- and time- dependent rheology

Marie Gautier,[a,b] Theany To,[a] Anne-Sophie Botte,[b] Jules Dupire,[b] Tanguy Rouxel*[a] and Franck Artzner*[a]

Univ Rennes, CNRS, IPR (Institut de Physique de Rennes) - UMR 6251, F-35000 Rennes, France

CHANEL Parfums Beauté, IR&D, 93500 Pantin, France

*Corresponding authors: tanguy.rouxel@univ-rennes.fr (T. Rouxel); franck.artzner@univ-rennes.fr (F. Artzner).

Table of contents

SI 1. Detailed LAOS rheology methodology

Small Amplitude Oscillatory Shear (SAOS). In the LVE zone, the shear stress response to a sinusoidal strain also takes a sinusoidal signal $\tau(t) = \tau_0 \sin(\omega t + \delta)$, where τ_0 is the shear stress response amplitude and δ is the phase shift (also referred to as the loss angle). The storage modulus G' (real part of $G^*(t)$) and the loss modulus G'' (imaginary part of $G^*(t)$), as well as the loss factor $\tan(\delta)$, can be determined from the complex shear modulus $G^*(t) = \frac{\tau(t)}{\gamma(t)}$. The LVE zone is characterized by a plateau in the storage modulus G' at small strain amplitudes and displays the intrinsic rheological properties of the samples.[1]

Large Amplitude Oscillatory Shear (LAOS). Exiting the LVE zone is associated with a decrease in $\mathbf{G'}$ and $\mathbf{G''}$, indicating that the material begins to deform.[2] In this non-linear zone, the stress response to a sinusoidal strain signal is no longer sinusoidal.[3] In the frequential domain, it implies that, in addition to the fundamental frequency, higher harmonics begin to affect the signal. In this case, the shear stress response takes the form $\boldsymbol{\tau(t) = \sum_{n=1}^{\infty} \tau_n \sin(n\omega t + \delta_n)}$, where $\mathbf{n}$ represents higher-order harmonics, $\boldsymbol{\tau_n}$ and $\boldsymbol{\delta_n}$ are the corresponding amplitudes and phase angles of the shear stress response, respectively, and $\boldsymbol{\omega}$ is the pulsation of the applied oscillatory strain ($\boldsymbol{\omega = 2\pi f}$, where $\mathbf{f}$ is the frequency).

In this study, we focus on the first and third harmonics of the stress response. Indeed, the magnitudes of the higher-order harmonics are negligible and even-order harmonics have a magnitude of zero due to the rotational symmetry of the experiment. However, it is noteworthy that some studies have indicated that a non-zero value for the second-order harmonic magnitude may serve as an indicator for slippage or of imperfect alignment of the plates of the rheometer, and can also be associated with instrument noise.[3,4]

Several techniques were developed to analyze and interpret the non-sinusoidal shear stress response. For qualitative interpretation, Lissajous-Bowditch curves are often useful to catch the effect of frequency and amplitude on the non-linear response. Strain-stress curves characterize elastic contribution to the non-linear response while strain rate-stress curves reveal the viscous contribution.[5] The shape of these Lissajous-Bowditch curves allows for a visual interpretation of the non-linear behavior in terms of shear-thinning or shear-thickening, as well as strain-softening or strain-stiffening.[5,6] For a quantitative interpretation, the most common technique is the Fourier Transform (FT) rheology. The non-linear stress response can be developed in a Fourier series according to Eq.1, with G'_n and G''_n the Fourier coefficients. This method allows to express the time-dependent stress response into a Fourier space, displaying the amplitudes and phases of the periodic contributions as a function of frequency.[7]

$$\tau(t) = \gamma_0 \sum_{n=1}^{\infty} G'_n(\omega, \gamma_0) \sin(n\omega t) + G''_n(\omega, \gamma_0) \cos(n\omega t) \quad (1)$$

, where n is an odd integer

By analyzing the evolution of higher-order harmonic contributions relative to the fundamental frequency, it is possible to compare the non-linear response of different lipsticks.[7,8] To provide a physical insight into the quantitative non-linear behavior of the studied material and analyze the intracycle non-linearities, the Chebyshev decomposition derived from the Fourier coefficients is employed. As expressed in Eq. 2, the Chebyshev coefficients describe the intracycle changes in the elastic and viscous properties by mathematically representing the nonlinear shape of the stress response.[9–11] Nevertheless, the Chebyshev decomposition raises difficulty of physical interpretation due to potential singularities

inherent in its mathematical definition. To better capture non-linearities, a strain-stiffening ratio S (Eq. 3) and a shear-thickening ratio T (Eq. 4), based on the Chebyshev coefficients, were further proposed by Ewoldt et al.[5] These ratios can also be determined from the Lissajous-Bowditch curves and interpreted in terms of non-linear behavior. A positive S value indicates strain-stiffening, whereas a negative S value signifies strain-softening. Similarly, a positive T value denotes shear-thickening, while a negative T value indicates shear-thinning.

$$e_n = G'_n(-1)^{\frac{n-1}{2}} \quad , \quad v_n = \frac{G''_n}{\omega} \qquad (n: \text{odd integer}) \tag{2}$$

$$S = \frac{4e_3 + \cdots}{e_1 + e_3 + \cdots} = \frac{G'_L - G'_M}{G'_L} \tag{3}$$

and

$$T = \frac{4v_3 + \cdots}{v_1 + v_3 + \cdots} = \frac{\eta'_L - \eta'_M}{\eta'_L} \tag{4}$$

Where e_1 and e_3 are the first order and third order elastic Chebyshev coefficients, respectively. G'_M is the minimum-strain modulus or tangent modulus at minimum strain and G'_L is the large-strain modulus or secant modulus at the maximum strain. v_1 and v_3 are the first order and third order viscous Chebyshev coefficients, respectively. η'_M is the local viscosity at the minimum shear rate or tangent modulus at minimum shear rate and η'_L is the local viscosity at the maximum shear rate or secant modulus at maximum shear rate, both measured at a specific time point of the oscillation cycle.[12]

References

1 B. A. Macias-Rodriguez and A. A. Marangoni, *Crit Rev Food Sci Nutr*, 2018, 58, 2398–2415.

2 B. A. Macias-Rodriguez, in *Structure-Function Analysis of Edible Fats*, Elsevier Inc., 2019, pp. 169–195.

3 K. Hyun, M. Wilhelm, C. O. Klein, K. S. Cho, J. G. Nam, K. H. Ahn, S. J. Lee, R. H. Ewoldt and G. H. McKinley, *Progress in Polymer Science (Oxford)*, 2011, 36, 1697–1753.

4 C. Fischer, C. J. G. Plummer, V. Michaud, P. E. Bourban and J. A. E. Månson, *Rheol Acta*, 2007, 46, 1099–1108.

5 R. H. Ewoldt, G. H. McKinley and A. E. Hosoi, *J Rheol (N Y N Y)*, 2008, 52, 1427–1458.

6 S. Pan and N. Germann, *Thermochim Acta*, 2019, 679, 178332.

7 M. Wilhelm, *Macromol Mater Eng*, 2002, 287, 83–105.

8 B. A. Macias-Rodriguez and A. G. Marangoni, *Rheol Acta*, 2016, 55, 767–779.

9 R. H. Ewoldt, *J Rheol (N Y N Y)*, 2013, 57, 177–195.

10 A. M. Le, M. Y. Erturk and J. Kokini, *J Food Eng*, 2023, 336, 111193.

11 M. Y. Erturk, S. A. Rogers and J. Kokini, *Food Hydrocoll*, 2022, 128, 107558.

12 S. Pan and N. Germann, *Acta Mech*, 2020, 231, 3031–3042.

SI 2. Microstructure and its influence on rheological behavior

A strong link between microstructure and viscoelastic moduli was observed across the three lipstick grades. Under rapid cooling conditions, the microstructure in characterized by small crystals densely packed in small aggregates, leading to a larger storage modulus. In contrast, slow cooling results in the formation of larger crystals arranged into loosely connected aggregates, causing a significant reduction in both storage and loss moduli. These findings confirm that a dense network, composed of interconnected small crystals, enhances the rheological properties, yielding increased stiffness (Figure SI2.1).

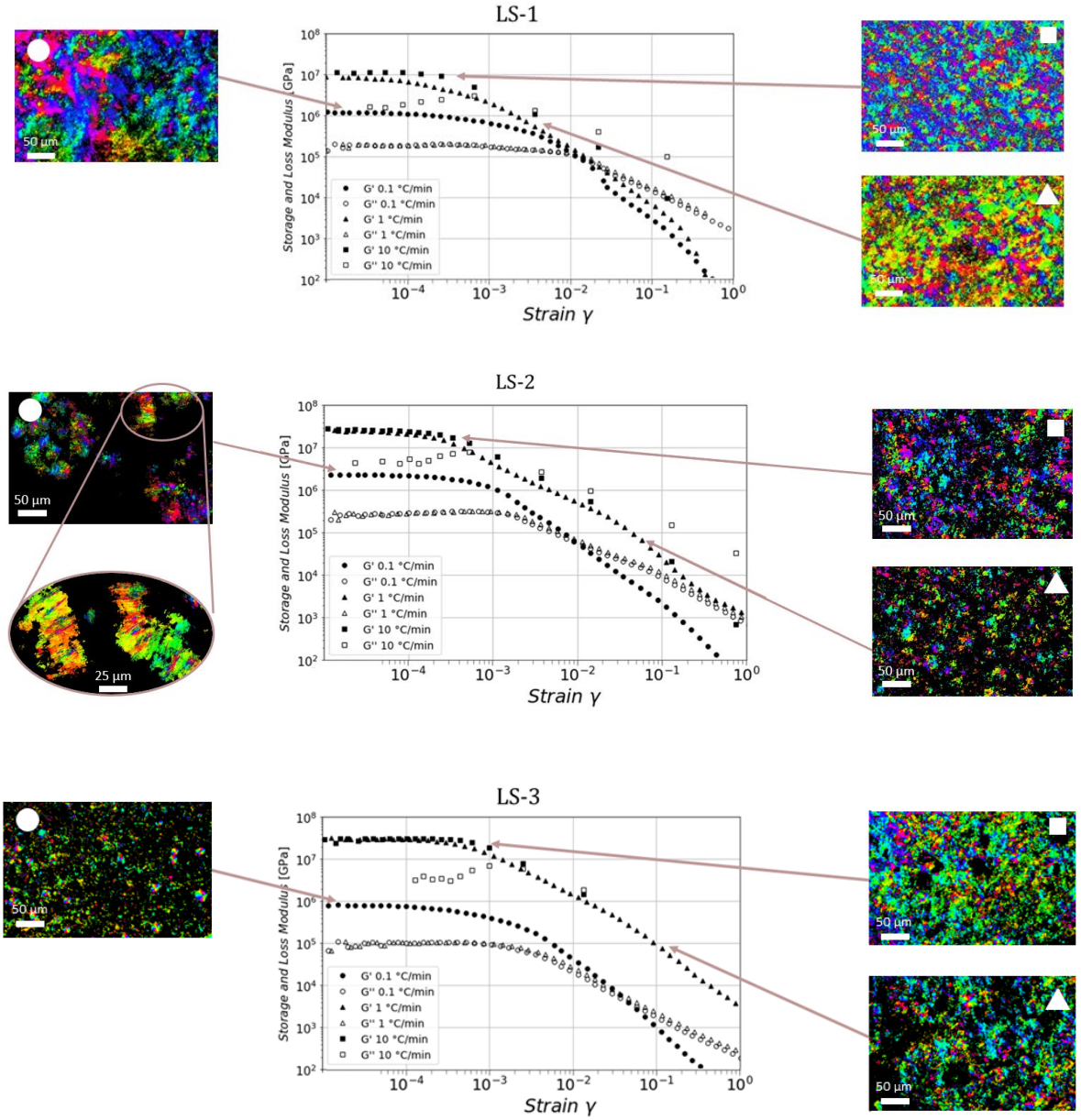

Figure SI2.1. Rheological oscillatory strain amplitude sweeps at 20 °C of LS-1, LS-2 and LS-3 samples (top to bottom) subjected to three cooling rates 0.1 °C. min^{-1} (circles), 1 °C. min^{-1} (triangles) and 10 °C. min^{-1} (squares) and corresponding LC-PolScope micrographs.

SI 3. Fourier-Transform Rheology - Spectral representation of the contribution of additional harmonics

As a material enters its NLVE zone, its stress response to a sinusoidal strain solicitation is no longer purely sinusoidal. In this regime, additional harmonics begin to emerge. The L-B curves reflect these new contributions to the material's behavior, typically including the third harmonic and, in some cases, the fifth harmonic as well. Even-order harmonics, however, do not contribute due to the symmetry of the experimental setup. To perform a quantitative analysis of the LAOS stress response, we convert the temporal signal into a Fourier space and examine the contribution of additional harmonics in a spectral representation, as shown in Fig. SI3.1 for $\gamma = 7 \times 10^{-2}$.

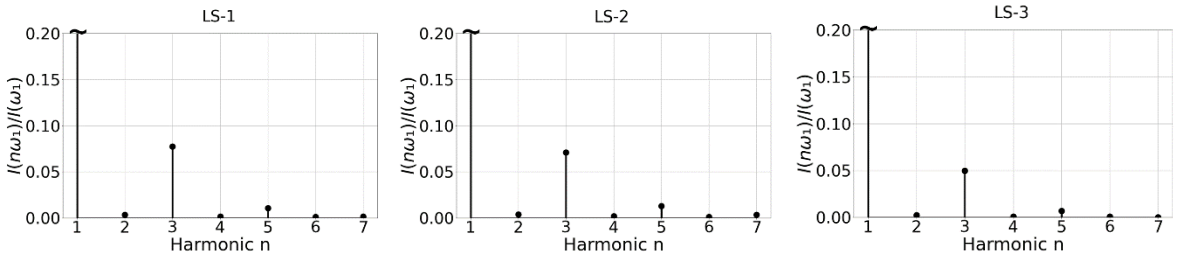

Figure SI3.1. Spectral representation of the contribution of additional harmonics to the stress response signal in Fourier space, at a frequency of 1 Hz and a strain of 7×10^{-2}. The magnitudes of the harmonics are normalized to the magnitude of the fundamental which is normalized to one.

SI 4. Comparison of rheological models

A KWW function-based creep model was selected to describe the rheological behavior of lipsticks in the linear regime (EqSI4.7).

We also considered less complex models during model development, including a simple Burgers model comprising a Maxwell element and a single Kelvin-Voigt element in series (EqSI4.1) as well as a generalized Burgers model, consisting of a Maxwell element in series with two Kelvin-Voigt elements (EqSI4.2), and the Zener model, also known as Standard linear solid model, comprising a Maxwell element in parallel with a spring (EqSI4.4). However, qualitative analysis of the model fits revealed that these models provide a significantly poorer fit, particularly at short timescales.

Quantitatively, all alternative models resulted in Root Sum of Squares (RSS) errors larger than that of the KWW creep model (Tab. SI4) while employing a greater number of parameters, indicating their inadequacy in accurately capturing the response to loading. Additionally, we evaluated the three-relaxation-time generalized Burgers model (EqSI4.3), but the inclusion of an extra discrete relaxation time did not yield significant improvement in fit quality, as shown by the RSS errors in Tab. S4. The Maxwell fractional model (EqSI4.5) could not capture the creep behavior either. We observe that the KWW model is improved when a viscosity term is added to the creep compliance equation. The residuals from fitting the two-relaxation-time Burgers model and the KWW-based model are plotted in Figure SI4.8.

Burgers model:

$$J(t) = \frac{1}{G_0} + \frac{1}{G_1}\left(1 - e^{-\frac{G_1 t}{\eta_1}}\right) + \frac{t}{\eta_0} \qquad \text{(Eq SI4.1)}$$

Two-relaxation-time generalized Burgers model:

$$J(t) = \frac{1}{G_0} + \frac{1}{G_1}\left(1 - e^{-\frac{G_1 t}{\eta_1}}\right) + \frac{1}{G_2}\left(1 - e^{-\frac{G_2 t}{\eta_2}}\right) + \frac{t}{\eta_0} \qquad \text{(Eq SI4.2)}$$

Three-relaxation-time generalized Burgers model:

$$J(t) = \frac{1}{G_0} + \frac{1}{G_1}\left(1 - e^{-\frac{G_1 t}{\eta_1}}\right) + \frac{1}{G_2}\left(1 - e^{-\frac{G_2 t}{\eta_2}}\right) + \frac{1}{G_3}\left(1 - e^{-\frac{G_3 t}{\eta_3}}\right) + \frac{t}{\eta_0} \qquad \text{(Eq SI4.3)}$$

Zener model:

$$J(t) = \frac{1}{G_0} + \left(\frac{1}{G_1} - \frac{1}{G_0}\right)\left(1 - e^{-\frac{G_1 t}{\eta_1}}\right) \qquad \text{(Eq SI4.4)}$$

Fractional Maxwell model:

$$J(t) = \frac{1}{G} + \frac{t^{\alpha}}{\eta_{\alpha}\Gamma(1+\alpha)} \qquad \text{(Eq SI4.5)}$$

KWW model or stretched exponential creep model, without viscosity term: (Eq SI4.6)

$$J(t) = \frac{1}{G_0} + \frac{1}{G_1}\left(1 - e^{-\left(\frac{t}{\tau}\right)^{\beta}}\right)$$

KWW model or stretched exponential creep model, with viscosity term:

$$J(t) = \frac{1}{G_0} + \frac{1}{G_1}\left(1 - e^{-\left(\frac{t}{\tau}\right)^{\beta}}\right) + \frac{t}{\eta_0} \quad \text{(Eq SI4.7)}$$

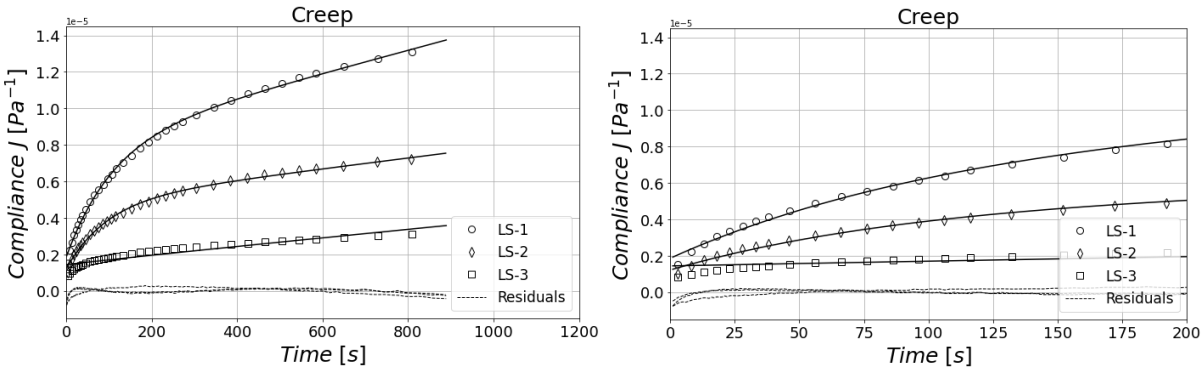

Figure SI4.1. Creep compliance curves under a 250 Pa shear stress, fitted using the **Burgers model**. The full-time response is shown (left), along with a zoomed-in view of the short-time response (right). Experimental data are shown with empty markers, while solid lines represent model predictions. Dashed lines show the residuals.

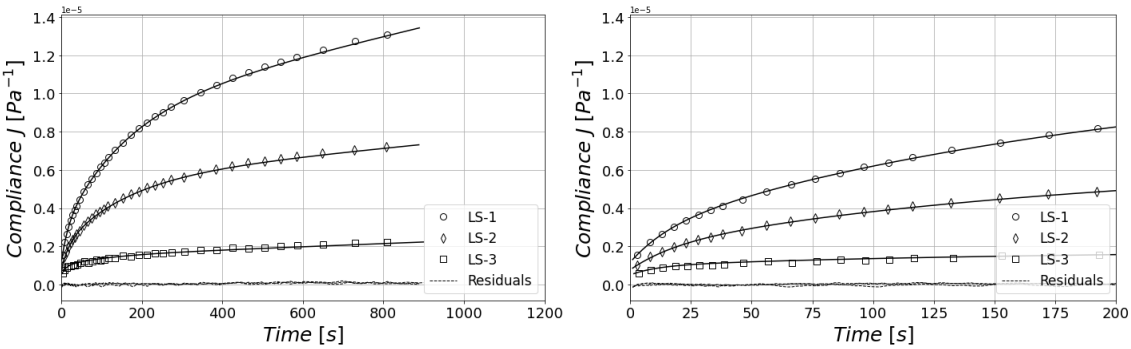

Figure SI4.2. Creep compliance curves under a 250 Pa shear stress, fitted using the **two-relaxation-time generalized Burgers model**. The full-time response is shown (left), along with a zoomed-in view of the short-time response (right). Experimental data are shown with empty markers, while solid lines represent model predictions. Dashed lines show the residuals.

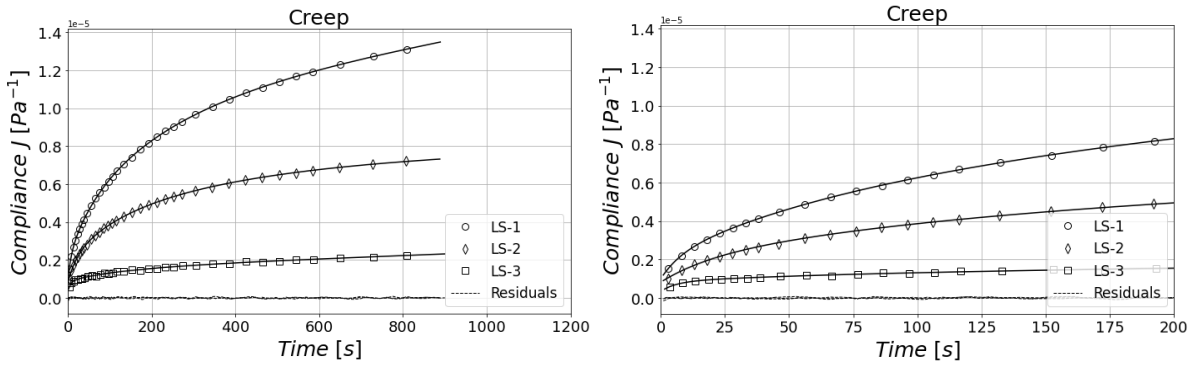

Figure SI4.3. Creep compliance curves under a 250 Pa shear stress, fitted using the **three-relaxation-time generalized Burgers model**. The full-time response is shown (left), along with a zoomed-in view of the short-time response (right). Experimental data are shown with empty markers, while solid lines represent model predictions. Dashed lines show the residuals.

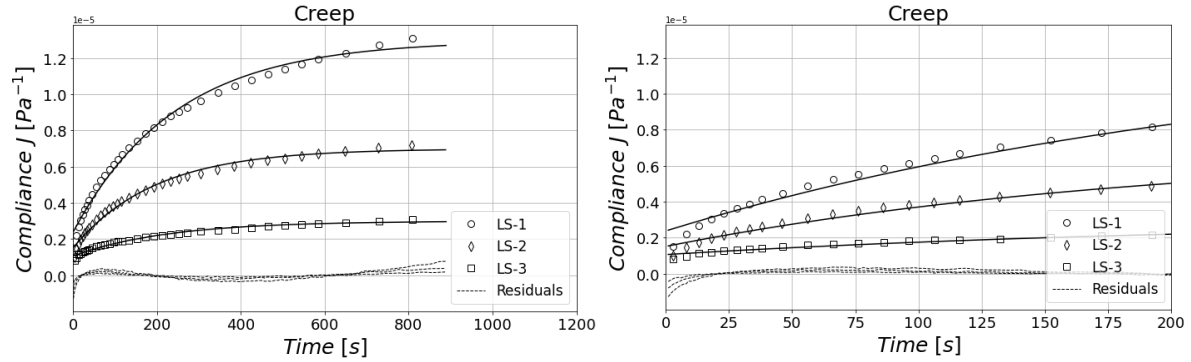

Figure SI4.4. Creep compliance curves under a 250 Pa shear stress, fitted using the **Zener model**. The full-time response is shown (left), along with a zoomed-in view of the short-time response (right). Experimental data are shown with empty markers, while solid lines represent model predictions. Dashed lines show the residuals.

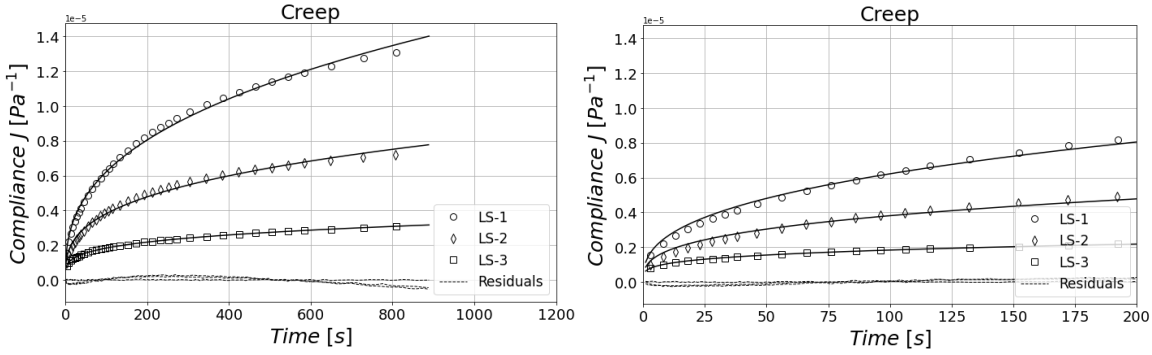

Figure SI4.5. Creep compliance curves under a 250 Pa shear stress, fitted using the **Fractional Maxwell model**. The full-time response is shown (left), along with a zoomed-in view of the short-time response (right). Experimental data are shown with empty markers, while solid lines represent model predictions. Dashed lines show the residuals.

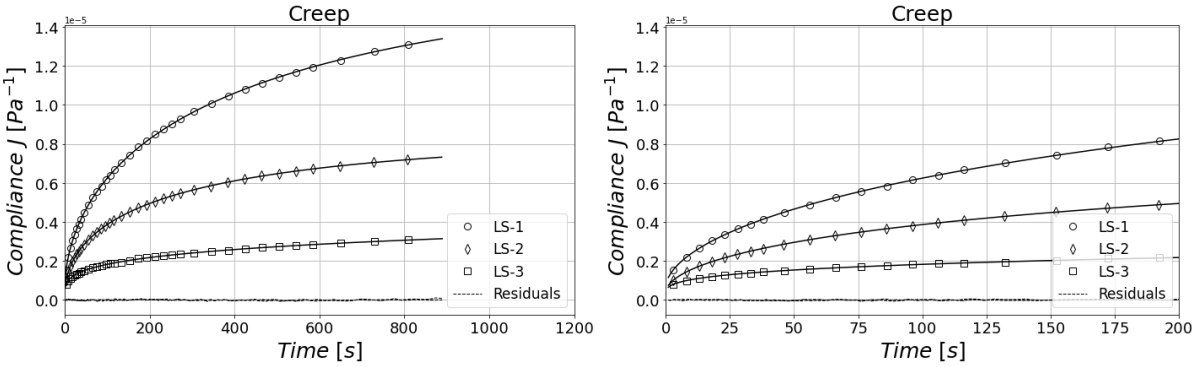

Figure SI4.6. Creep compliance curves under a 250 Pa shear stress, fitted using the **Kohlrausch Williams Watt (KWW) model (without viscosity term)**. The full-time response is shown (left), along with a zoomed-in view of the short-time response (right). Experimental data are shown with empty markers, while solid lines represent model predictions. Dashed lines show the residuals.

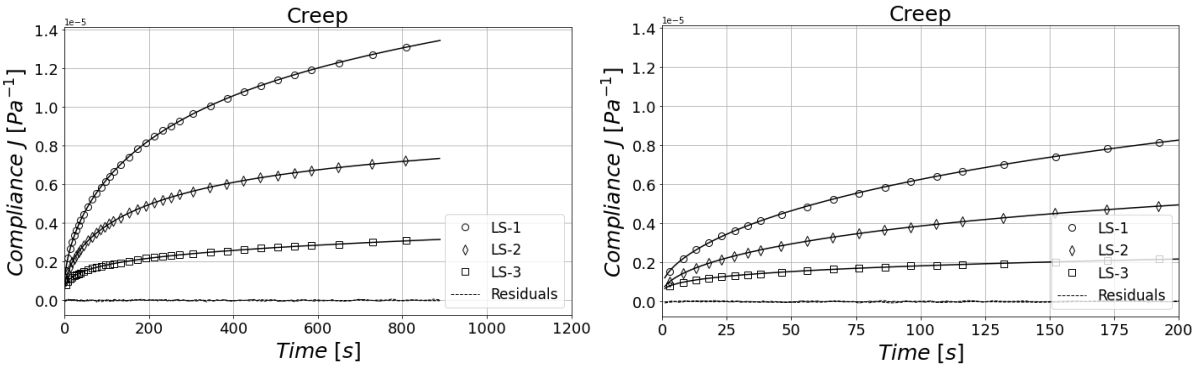

Figure SI4.7. Creep compliance curves under a 250 Pa shear stress, fitted using the **Kohlrausch Williams Watt (KWW) model (with viscosity term)**. The full-time response is shown (left), along with a zoomed-in view of the short-time response (right). Experimental data are shown with empty markers, while solid lines represent model predictions. Dashed lines show the residuals.

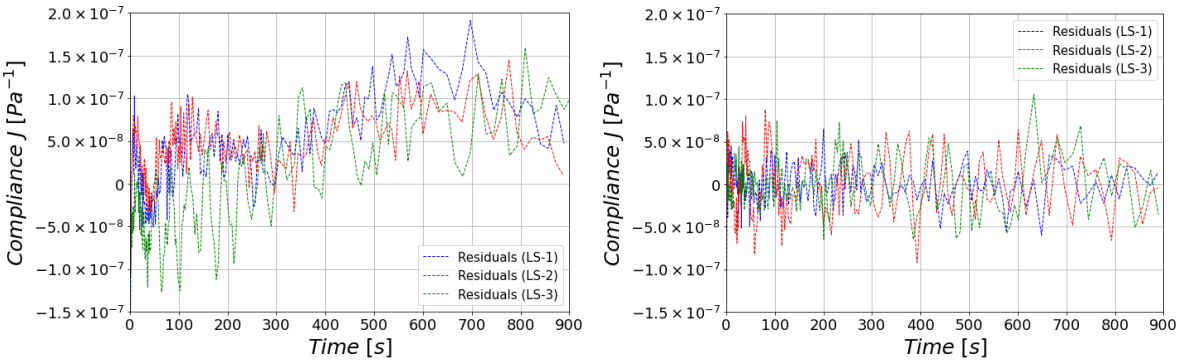

Figure SI4.8. Residuals from fitting the two-relaxation-time Burgers model (left) and the KWW-based model with a viscosity term (right) to the creep compliance data. The smaller residuals for the KWW model indicate a better fit and improved description of the material's relaxation behavior.

Table SI4. Root Sum of Squares (RSS) errors obtained from fitting the simple Burgers model, the two-relaxation-time generalized Burgers model, the three-relaxation-time generalized Burgers model, the Zener model, the fractional Maxwell model, and the KWW creep model (with and without a viscosity term) to samples LS-1, LS-2 and LS-3

	Number of parameters	LS-1	LS-2	LS-3
Burgers Model – RSS Error	4	1.9×10^{-6}	1.3×10^{-6}	3.1×10^{-6}
Two-relaxation-time Generalized Burgers Model – RSS Error	6	4.6×10^{-7}	5.2×10^{-7}	4.8×10^{-7}
Three-relaxation-time Generalized Burgers Model – RSS Error	8	3.2×10^{-7}	4.2×10^{-7}	5.0×10^{-7}
Zener Model – RSS Error	3	4.3×10^{-6}	2.6×10^{-6}	1.2×10^{-6}
Fractional Maxwell model – RSS Error	3	2.8×10^{-6}	2.2×10^{-6}	3.0×10^{-7}
KWW model (no viscosity) – RSS Error	3	4.3×10^{-7}	3.1×10^{-7}	2.9×10^{-7}
KWW model (with viscosity) – RSS Error	**4**	$\mathbf{3.7 \times 10^{-7}}$	$\mathbf{2.9 \times 10^{-7}}$	$\mathbf{2.7 \times 10^{-7}}$

SI 5. Inventory of raw data corresponding to figures

Figure	Data File Name	Description
Figure 5	Experimental data (numerical values) ampsweep_depending_on_cooling_rate.csv	Raw rheological measurements (amplitude sweeps) of the three samples cooled at three different cooling rates ($0.1\ °C.\ min^{-1}$, $1\ °C.\ min^{-1}$ and $10\ °C.\ min^{-1}$).
Figure 7	Experimental data (numerical values) ampsweep_1Hz.csv ampsweep_1Hz_2.csv	Raw rheological measurements (strain amplitude sweeps) of the three samples at 1 Hz and room temperature.
Figure 8	Experimental data (numerical values) Freqsweep.csv Freqsweep_2.csv	Raw rheological measurements (frequency sweeps) of the three samples at 0.01% strain amplitude and room temperature.
Figure 12	Experimental data (numerical values) Creep_recovery_strain.csv Creep_recovery_strain_2.csv	Raw creep and recovery strain measurements of the three samples under 250 Pa stress and at room temperature.
Figure 13	Experimental data (numerical values) Creep_recovery_Compliance.csv Creep_recovery_Compliance_2.csv Python code for model fitting KWW_creep_model.py	Raw creep and recovery compliance measurements of the three samples under 250 Pa stress and at room temperature. Python code used to fit the KWW based creep model to the experimental data, developed specifically for this study.
Figure 14	Experimental data (numerical values) Compression_data_14a_10µms.csv Compression_data_14a_10µms_2.csv Compression_data_14b_5000µms.csv Compression_data_14b_5000µms_2.csv	Raw uniaxial compression measurements of the three samples at room temperature and at two different compression rates (10 µm/s and 5000 µm/s).
Figure 15	Video files LS-1_compression.gif LS-2_compression.gif LS-3_compression.gif	Videos of the compression measurements and cracking of the three samples at room temperature and at a 10 µm/s compression rate.